A Combined EXAFS and Diffraction Study of Pure and Doped Nanocrystalline Tin Oxide

Steven R. Davis, Alan V. Chadwick,* and John D. Wright

Centre for Materials Research, Chemistry Department, University of Kent, Canterbury, Kent CT2 7NH, U.K.

Received: May 30, 1997; In Final Form: July 26, 1997[⊗]

Nanocrystals of pure, Cu^{2+} and Fe^{3+} doped SnO_2 have been prepared by a sol−gel route and were investigated by a combination of EXAFS and XRPD measurements. Surface doped samples were also studied, and these were prepared by immersing pure nanocrystals in aqueous solutions of the dopant cations. The XRPD results showed the average size of the crystallites when freshly prepared was 2−3 nm and was not affected by the dopant. The Sn K-edge EXAFS of the pure SnO_2 nanocrystals was consistent with their size and suggested the level of disorder in the crystallites was comparable to that in bulk SnO_2. The K-edge EXAFS of the dopants showed that up to at least 10 mol % nominal doping of both Cu^{2+} and Fe^{3+} ions in sol−gel prepared samples were situated on Sn^{4+} sites in the SnO_2 cassiterite lattice. In the case of the surface doped samples the EXAFS showed no penetration of the dopant into the SnO_2 lattice. The growth of the crystallites on heating was monitored by XRPD and was found to become clearly evident at about 400 °C. The effect of the dopants was to lower the growth rate of the nanocrystals. Heating the doped sol−gel prepared samples yielded EXAFS spectra that indicated the dopants gradually moved to surface regions of the crystallites. In the case of the nominally 10 mol % Fe^{3+} doped sample, heating for 1 h at 900 °C caused the precipitation of iron oxide. Heating the surface doped samples up to 900 °C did not cause a penetration of the dopant into the SnO_2 lattice.

1. Introduction

There is a growing interest in nanocrystalline materials since their properties can be markedly different from the parent bulk solids.[1−4] Reasons for the interest in nanocrystalline oxides include the possibilities of producing superhard and superplastic ceramics and catalysts with enhanced activities. Clearly, the increased surface area to volume ratio afforded by preparing a catalyst in nanocrystalline form will increase activity; however, recent work on simple binary oxides[5−7] suggests other factors, i.e., surface morphology and surface chemistry, are advantageously different for nanocrystals. In addition, nanocrystalline materials will dissolve higher concentrations of impurities than their bulk counterparts, and this offers further scope for tailoring new catalytic materials. A detailed understanding of the chemistry of these new materials is reliant on a detailed characterization, and in this paper we report new structural information on pure and doped nanocrystalline tin oxide, SnO_2.

Tin oxide is an *n*-type semiconductor which is widely used as an oxidation catalyst and forms the active element of flammable gas sensors.[8−10] The basis of the gas sensors is that the surface resistance of an SnO_2 pellet at elevated temperatures decreases in the presence of flammable gases as they react with chemisorbed oxygen releasing electrons into the solid surface. Several routes exist to nanocrystalline SnO_2, including sol−gel synthesis[11,12] and vacuum sputtering,[13,14] and these have been used to produce materials with improved catalytic and sensing performance. The sol−gel route offers a simple method of incorporating dopants into the material and enhancing the selectivity of SnO_2 in both applications. For example, doping SnO_2 with Cu^{2+} cations promotes the oxidation of carbon monoxide by oxygen or nitric oxide,[15,16] and the material has a proposed application as an emission control catalyst for automotive vehicles.[17] A wide variety of cationic dopants have been used to improve the selectivity of SnO_2 gas sensors, and it is worth noting that Cu^{2+} doping has been claimed to enhance the detection of hydrogen sulfide.[18]

Extended X-ray absorption fine structure (EXAFS) spectroscopy is a local structural probe which enables the structure around a specific atom to be determined accurately.[19−21] EXAFS, unlike Bragg diffraction, does not rely on long-range order and can be used to study local structure in liquids and amorphous and crystalline solids. A number of nanocrystalline, binary metal oxides have been characterized by EXAFS, including ZnO,[22−24] ZrO_2,[25,26] and SnO_2.[27−29] The type of information that has been deduced has been particle sizes, bond lengths, dynamics within the particles, and the location of dopants.

In this study we have measured the X-ray powder diffraction (XRPD) patterns and the EXAFS at the cation K-edges in pure and Cu^{2+} and Fe^{3+} doped SnO_2 prepared as nanocrystals by a sol−gel route. The measurements were made on samples that had been subjected to a variety of thermal treatments. The sol−gel route is well-known to produce crystallites of a few nanometers in diameter, the exact dimensions depending on the drying conditions.[27,29] Although a detailed analysis of the Sn K-edge EXAFS data can be used to estimate particle size,[27] we have used XRPD as the primary means of determining the average crystallite radius as it is subject to fewer assumptions in the analysis. The EXAFS of the dopant cations was used to locate the positions of these ions, a role for which the technique is particularly well-suited.[30] The only previous study[31] of the location of Cu^{2+} ions in SnO_2 employed EPR methods and indicated that the dopant in sol−gel prepared samples was initially situated both in surface sites and within the bulk SnO_2 lattice, the latter site dominating after the samples were calcined at temperatures between 300 and 800 °C. A slightly different picture emerges from the present study. There has been an EXAFS study[32] of Fe_2O_3−SnO_2 with measurements at both the Sn and Fe K-edges; however, the minimum concentration of Fe was 33 mol %, and therefore the data are not comparable with those in the present study.

* To whom correspondence should be addressed.

⊗ Abstract published in *Advance ACS Abstracts,* October 15, 1997.

S1089-5647(97)01756-2 CCC: $14.00 © 1997 American Chemical Society

2. Experimental Section

2.1. Materials Preparation. The preparation followed the method of Ansari et al.,[12] A 0.1 M solution of tin chloride pentahydrate (Aldrich, 98% purity) was prepared by dissolving 1.402 g in 40 mL of distilled water. To this solution, 5 mL of aqueous ammonia (0.880 w/w, Fisons) was added, and the solid from the resulting gel was recovered by evaporation. The ammonium chloride byproduct was removed by extensive washing with distilled water. The washed material was dried in an oven at 100 °C overnight and ground in an agate mortar and pestle. The X-ray powder diffraction pattern confirmed the material was nanocrystalline tin oxide.

Cationic dopants were introduced by adding the appropriate amount of the metal chloride ($CuCl_2$ and $FeCl_3$) to the initial tin chloride solution and following the above procedure. Samples were prepared with nominal dopant concentrations of 1, 5, and 10 mol % for copper and iron.

For comparative purposes samples of the pure nanocrystalline SnO_2 were suspended in aqueous solutions of $CuCl_2$ and $FeCl_3$, filtered, and dried at 100 °C. These samples were assumed to be surface doped, as in previous studies.[31]

2.2. Laboratory X-ray Powder Diffraction. X-ray powder diffraction patterns of all of the samples were collected on a Phillips PW1050 powder diffractometer. Particle sizes, *S*, were determined from the Debye−Scherrer equation;[33] i.e.

$$S = \frac{K\lambda}{\beta \cos \theta}$$

where *K* is a constant (0.89), β is the full width at half-maximum height of a diffraction peak at angle θ, and λ is the X-ray wavelength (in the present work Cu Kα radiation was employed).

2.3. Combined EXAFS and X-ray Powder Diffraction. Measurements were made on station 9.3 at the CLRC Daresbury Synchrotron Radiation Source. The synchrotron has an electron energy of 2 GeV, and the average current during the measurements was 150 mA. Station 9.3 is designed specifically for combined EXAFS and XRPD measurements. It is equipped with a high-stability, double Si (220) crystal monochromator which can be offset from the Bragg angle to reject harmonic contaminants from the monochromatic beam. In the present work the harmonic rejection was set at 50%. The station will run in "quick" EXAFS mode. EXAFS spectra for concentrated samples can be collected in transmission mode using gas-filled ion chamber detectors. For dilute samples spectra are collected in fluorescence mode, the signal being monitored with a multielement Canberra solid state detector. XRPD patterns can be collected immediately before or after an EXAFS spectrum on an INEL curved, position sensitive X-ray detector. EXAFS and XRPD data can be collected up to 1100 °C using a furnace specially designed for this station.[34]

The EXAFS/XRPD samples were prepared by thoroughly mixing the ground material with fumed silica and pressing into pellets in a 13 mm IR press. EXAFS spectra for the Sn K-edge were collected in transmission mode to $k = 16$ Å^{-1}. For these measurements the amount of sample in the pellet was adjusted to give an absorption of about $\mu d = 1$. Cu and Fe K-edge spectra were collected in fluorescence mode to $k = 14$ Å^{-1}. All of the data were collected by running the station in quick EXAFS mode, with typical collection times of 180 s for EXAFS and 120 s for XRPD. XRPD patterns were collected at 0.619 78 Å, the wavelength of the Mo absorption edge. In some cases several EXAFS scans were collected and averaged to improve the signal-to-noise ratio. The data were processed in the conventional manner using the Daresbury suite of EXAFS programs: EXCALIB, EXBACK, and EXCURV92.[35] Phase shifts were derived from ab initio calculations within EXCURV92. The data were Fourier filtered to include the region of 1−5 Å of the Fourier transform containing the dominant peaks. For each back-transformed spectrum a theoretical fit was obtained by adding shells of atoms around the central excited atom and iterating the radial distances, RD, and the Debye−Waller type factors, A ($=2\sigma^2$). This latter factor will contain contributions from both thermal disorder and static variations in RD. In the case of the Sn EXAFS the coordination number, CN, was also iterated. The quality of the fit is measured by an *R*-factor, given as a percentage,[35] and the errors in RD are ∼± 0.02 Å and ∼± 20% in *A* and CN.

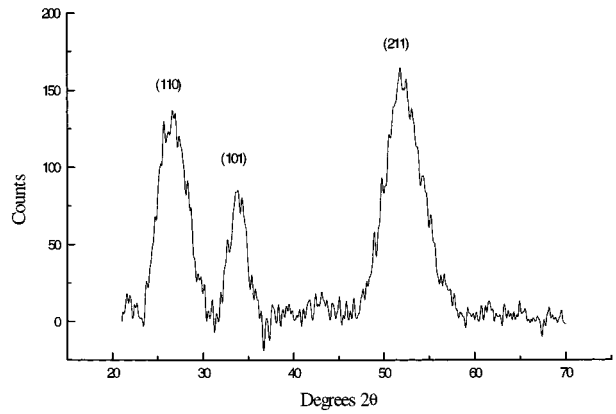

Figure 1. Laboratory XRPD pattern for pure, nanocrystalline tin oxide. The pattern was collected with Cu Kα radiation.

3. Results

A typical XRPD pattern for the tin oxide powders produced by the present preparation route is shown in Figure 1. The (110), (101), and (211) peaks are very broad, and the Debye−Scherrer equation yields an average particle size of 2−3 nm, confirming the nanocrystalline nature of the material. The same size was deduced from the reflections of different (*hkl*) values, suggesting the particles were of a regular shape with similar dimensions in each direction. The patterns for doped samples were similar and showed only peaks for tin oxide.

The effect of heating on the particle size of the nanocrystals was monitored in two types of experiment. Samples were subjected to fixed period, isothermal anneals at various temperatures up to 900 °C. The sizes of these samples were determined from laboratory XRPD patterns. In addition, samples were subjected to fixed rate heating on the combined EXAFS/XRPD station. Typical heating rates were 5 °C/min, and an XRPD pattern was collected over 2 min at 5 min intervals. The latter experiments yielded data more rapidly; however, both types of experiment showed that significant growth of the particles began at about 400 °C, which is consistent with previous work.[29] Typical XRPD patterns from the synchrotron experiments are shown in Figure 2. Figure 3 shows the particle sizes as a function of temperature for doped and undoped tin oxide collected in synchrotron experiments using the same heating conditions. After samples cooled, the XRPD patterns were collected at room temperature and the particle size determined. This showed that the increased Debye−Waller factor at high temperatures was not making a significant contribution to the line broadening. The shapes of the plots are all similar, significant growth occurring at around 400 °C and the growth rate accelerating with increasing temperature. The doped crystals do not grow as rapidly as the

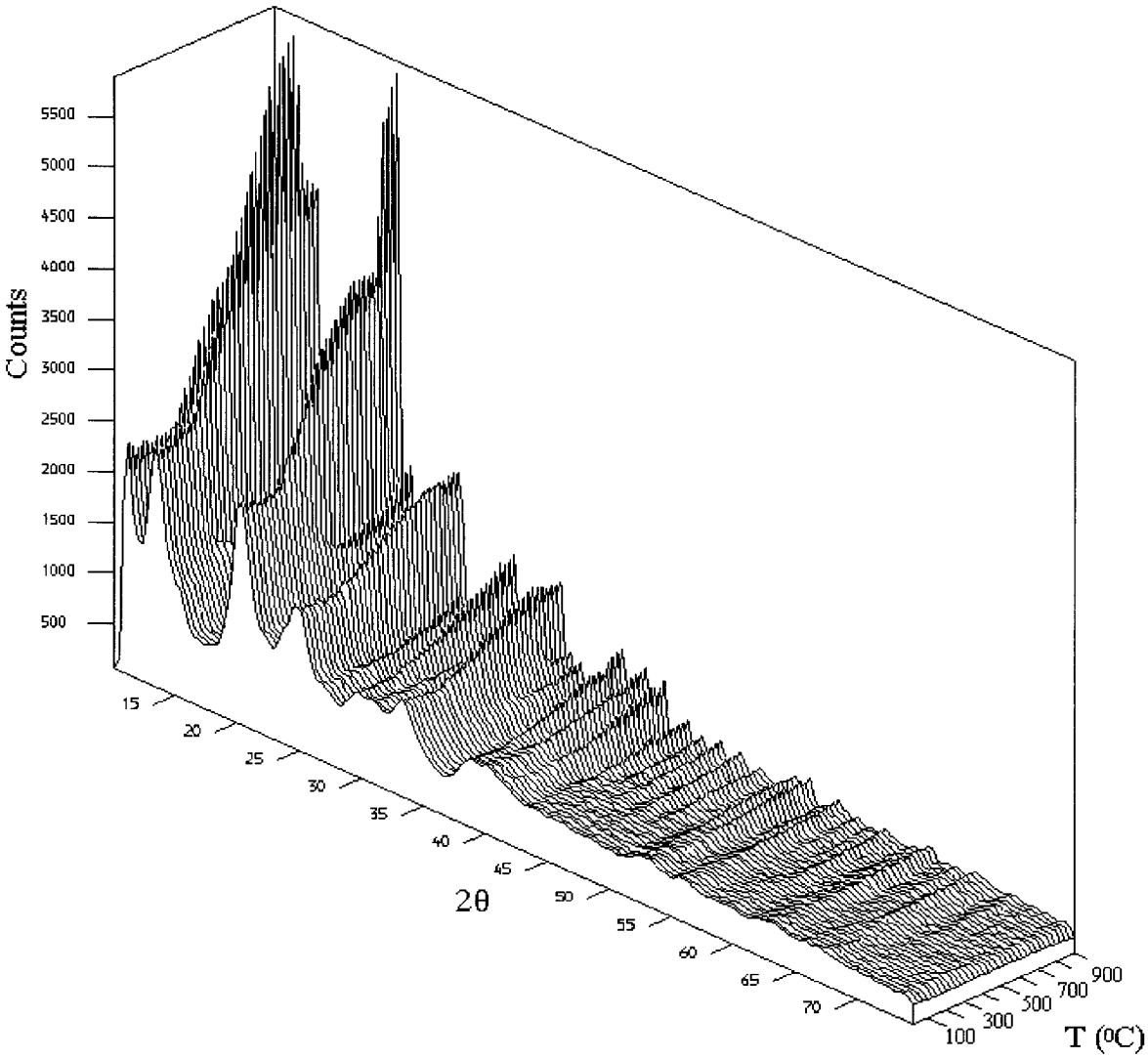

Figure 2. 3-D plot of the XRPD patterns for tin oxide collected on station 9.3. The heating rate was 5 °C/min with patterns collected over 2 min periods every 5 min. The pattern was collected at the Mo absorption edge.

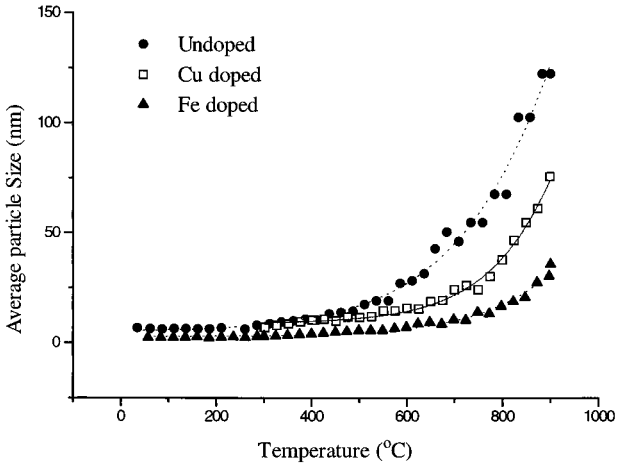

Figure 3. Dependence of particle size of various tin oxide samples during heating at 5 °C/min: (filled circles) pure tin oxide; (open squares) nominal 5 mol % Cu^{2+}; (filled triangles) nominal 5 mol % Fe^{3+}.

pure SnO_2, which is very marked in the case of Fe^{3+} doping, suggesting the dopants inhibit growth.

The Sn K-edge EXAFS of a bulk sample of pure tin oxide (particle size ~200 nm) was collected at room temperature, and the data are displayed in Figure 4. The raw data have been Fourier filtered to isolate the peaks between 1 and 5 Å in real space and back-transformed to yield the EXAFS shown. The data were fitted to a simple four shell model, and the final parameters are displayed in Table 1. In the fitting the coordination numbers were held constant at the values obtained in the crystallographic data.[36] The six nearest neighbor O atoms were considered as a single shell in the EXAFS as the slight differences in distances found in the diffraction data would not be resolved. The fit is good and the bond lengths agree well with the crystallographic data, to within the ±0.02 Å error expected in the EXAFS. This confirms the validity of the phase shifts used to analyze the data. It is worth noting that allowing the coordination numbers to vary in the fitting gives only a marginal improvement and the individual values of CN are within 20% of those from the crystallographic data.

The Sn K-edge EXAFS of a nanocrystalline sample of pure tin oxide (particle size 2−3 nm) at room temperature are shown in Figure 5. The data were treated using the same Fourier filtering procedure described above for the bulk sample. The striking features of these data are the reduced amplitude of the EXAFS oscillations and the concomitant reduced magnitude of the outer peaks in the Fourier transform. Similar EXAFS data have been reported for nanocrystalline SnO_2 and are expected for a nanocrystalline sample as a large fraction of Sn atoms will be in the surface and the *average* CN will be reduced for these shells. The data were fitted to two models. In the first

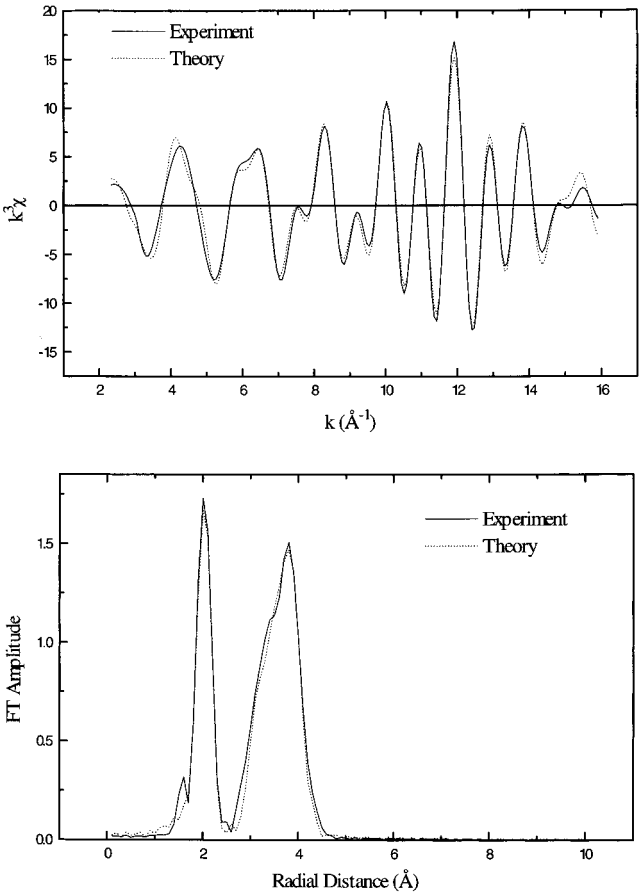

Figure 4. Sn K-edge EXAFS spectrum (k^3-weighted) for a bulk sample of tin oxide (a, top) and the corresponding Fourier transform (b, bottom) corrected with the phase shift of the first shell. The experimental data are the solid line, and the best fit is the dotted line.

model the CNs were the same as those for the bulk material. A good fit was obtained, and the parameters are listed in Table 1. In this case the reduction in magnitude of the peaks was accounted for by the increase in the Debye−Waller factors. The bond lengths are very close to those for the bulk material. In the second model the CNs were allowed to float in the fitting, and the best-fit parameters are given in Table 1. This is a more realistic approach to a nanocrystalline material; however, there are clearly difficulties in obtaining precise parameters with the increased number of variables and a limited data set. Given this precaution, the parameters are informative. The *R*-factor for the fit is improved, as would be expected, and the parameters on the whole are sensible. For the first shell there is a negligible reduction in CN to 5.8. The CNs of the outer shells are all reduced, as predicted. Parameters for the second O shell at ∼3.6 Å are not very reliable as it is a shell of weakly backscattering atoms and is making a minor contribution to the ExAFS. The value of CN is most reliable for the outermost Sn shell since the backscattering from this shell will be making a major contribution to the EXAFS due to the high atomic number of Sn. The value of CN of 4 is consistent with the size of the nanocrystals on the basis of a previous EXAFS study of nanocrystalline tin oxide.[27,29] We undertook further tests of the reliability of the parameters obtained from this second model. The individual shells for the Sn atoms were isolated by Fourier filtering and least-squares fitted with CN held constant and allowed to float. For each shell, the latter approach gave a considerably better fit and the parameters were very similar to those listed in Table 1 for the second model.

The present EXAFS data, and those in previous studies on even smaller SnO_2 crystallites than those studied here, i.e., ∼1−2 nm,[27,29] indicate that the tin oxide nanocrystals differ mainly in particle size from the bulk material. The bond lengths are very similar, and the similar Debye−Waller factors obtained in the second model suggest there is no major increase in either the dynamic or static disorder. These are important observations and remove some of the speculation on the nature of disorder in nanocrystals, at least for SnO_2. It should be emphasized once more that EXAFS is giving an average picture of the nanocrystal and it will not be very sensitive to the details of disorder that might be expected in the very outermost surface layers. However, recent calculations[37] indicate that even in the outermost layer of bulk SnO_2 the bond lengths only change by ∼0.1 Å and if similar changes were present in the surface of nanocrystals, they would be difficult to detect in EXAFS. We believe these observations for the pure material are important as they provide a foundation for understanding the doped samples in that the nanocrystals can be considered as regular lattices, without invoking high levels of disorder.

The Cu K-edge EXAFS were collected for several doped nanocrystalline tin oxide samples, and the data at room temperature were essentially independent of the dopant concentration, although the higher concentrations gave the better signal-to-noise ratio in the raw EXAFS. The data for the nominal 5 mol % doped samples are shown in Figure 6. The data were Fourier filtered to isolate the peaks between 1 and 5 Å. There are two dominant peaks, one at ∼2 Å and one at ∼4 Å, due to backscattering from oxygen and metal atoms, respectively. The EXAFS were clearly different from those for simple oxides of copper, suggesting that the Cu had substituted for Sn in the lattice. In CuO a large peak around 3 Å is seen in the Fourier transform of the Cu K-edge EXAFS due to a shell of 10 cations between 2.9 and 3.2 Å (see the data at the foot of Table 2). Such a peak is absent in the present spectrum. The data were therefore fitted to a simple lattice substitution model, and the parameters are listed in Table 2. The fit is good, and the parameters are sensible. There is some reduction in the Cu−Sn bond lengths compared to Sn−Sn bond lengths that would be expected due to the reduced Coulombic interactions resulting from replacing Sn^{4+} by Cu^{2+}. The Debye−Waller factors are higher than those for the Sn EXAFS of pure SnO_2. For the outer shells this is partly due to the use of fixed coordination numbers. There will also be a contribution from static disorder as the introduction of Cu^{2+} will be charge compensated by the introduction of O^{2-} vacancies. Given the more limited *k* range of the data, fitting with the CNs allowed to vary was not informative. Overall the EXAFS strongly supports the view that the method of preparation employed leads to nanocrystals of SnO_2 in which Cu has predominantly entered into the lattice by simple random substitution on the Sn sites.

The Cu K-edge EXAFS were collected at room temperature for doped samples that had been heated for 1 h at high temperatures. The Fourier transforms for several 5 mol % doped samples are shown in Figure 7. The significant feature of the plots is the decrease in the amplitude of the peak at ∼4 Å, due to outer shells, with increasing temperature. This indicates that at the higher temperatures, when the SnO_2 grains are increasing in size, the Cu atoms are moving to more statically disordered sites. Several possible models of these sites could be invoked, for example Cu atoms occupying both interstitial and substitutional sites, clustering of Cu atoms with point defects, etc. All of these models are difficult to test without more ancillary information. The simplest explanation, although it is speculative, is that the Cu atoms are in surface regions of the crystallites. This is not necessarily the outermost layer. There could be a rather deep disordered region where the crystallite has been

TABLE 1: EXAFS Results for Pure Tin Oxide

	X-ray[a]		EXAFS of bulk			EXAFS of nano[b]		
atom	CN	R/Å	CN	R/Å	A/Å^2	CN	R/Å	A/Å^2
O	2	2.045	6	2.050	0.005	6 (5.8)	2.045 (2.045)	0.009 (0.008)
O	4	2.088						
Sn	2	3.185	2	3.201	0.007	2 (1.0)	3.210 (3.206)	0.009 (0.005)
O	4	3.594	4	3.571	0.001	4 (2.8)	3.586 (3.429)	0.009 (0.041)
Sn	8	3.708	8	3.730	0.007	8 (4.0)	3.718 (3.716)	0.017 (0.010)
				R = 18.44%			R = 17.40% (14.92%)	

[a] From ref 36. [b] The data in parentheses are obtained by floating the coordination number.

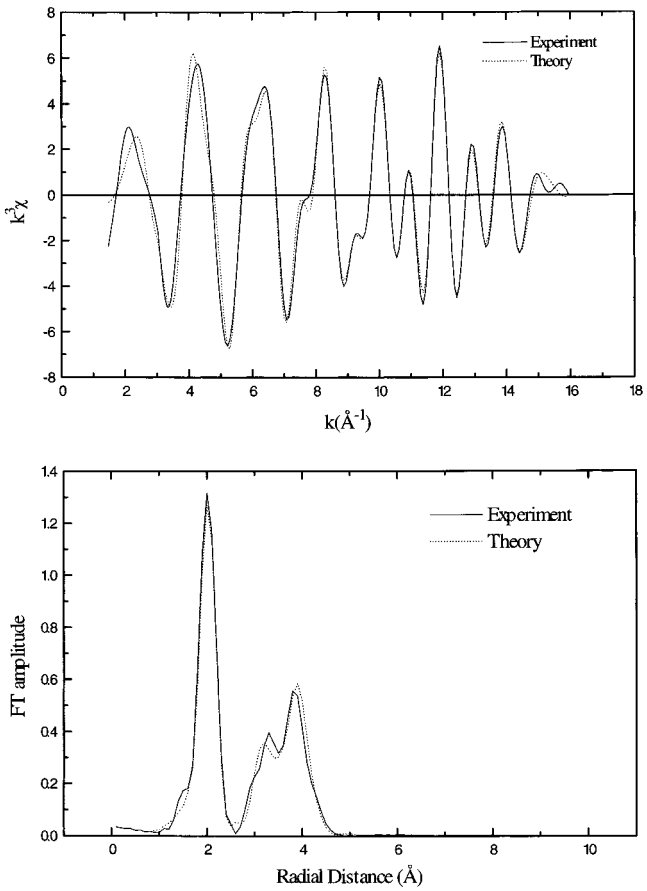

Figure 5. Sn K-edge EXAFS spectrum (k^3-weighted) for a nanocrystalline sample of tin oxide (a, top) and the corresponding Fourier transform (b, bottom) corrected with the phase shift of the first shell. The experimental data are the solid line, and the best fit is the dotted line.

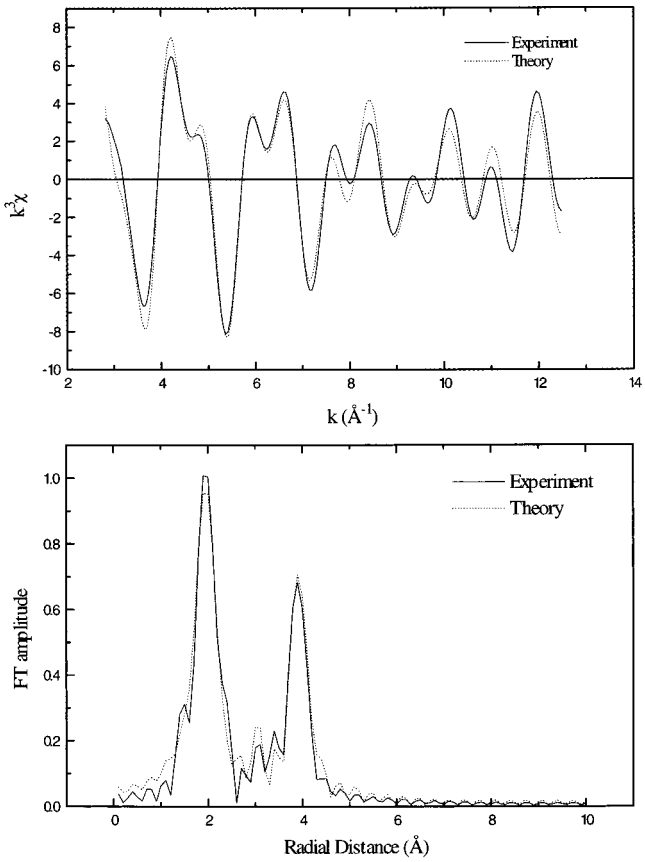

Figure 6. Cu K-edge EXAFS spectrum (k^3-weighted) for a nanocrystalline sample of nominally 5 mol % Cu doped tin oxide (a, top) and the corresponding Fourier transform (b, bottom) corrected with the phase shift of the first shell. The experimental data are the solid line, and the best fit is the dotted line.

undergoing growth. It is interesting to note that at the highest annealing temperature of 900 °C there is no evidence of the precipitation of CuO in the sample.

A comparison between the EXAFS of the sol−gel produced, bulk Cu^{2+} doped SnO_2 samples and the surface doped material is shown in Figure 8. The Fourier transform of the surface doped sample that had not been heated (labeled 25 °C in Figure 8) is similar to that of the bulk doped sample that had been heated for 1 h at 900 °C. This is strong supportive evidence that heating of the bulk doped samples causes a relocation of the Cu^{2+} to surface regions. Heating the surface doped sample to 900 °C resulted in an almost negligible peak at ∼4 Å and a small, broad peak around 3 Å. The absence of the ∼4 Å peak indicates that the Cu^{2+} cations have not penetrated the SnO_2 matrix. The weak peak at ∼3 Å may be the onset of the precipitation of CuO on the surface of the sample; however, the quality of the data was not sufficient for a detailed analysis.

The Fe K-edge EXAFS for the Fe^{3+} doped SnO_2 samples showed many similarities to the Cu K-edge EXAFS of the Cu^{2+} doped samples. The EXAFS and the Fourier transform for a nominally 5 mol % Fe^{3+} doped SnO_2 sample are shown in Figure 9. The data were Fourier filtered to isolate the dominant peaks at ∼2 and 4 Å. A very different Fourier transform is expected for simple iron oxides. For example, in Fe_2O_3 a large peak is present around 3 Å due to a shell of seven cations between 2.9 and 3.4 Å (see the data at the foot of Table 2). This peak is absent in the present spectrum. The best model fit was obtained by assuming that the Fe^{3+} substituted randomly on the Sn sites, and the best fit parameters are listed in Table 2. Heating the samples for 1 h at a series of temperatures and measuring the room temperature EXAFS produced the data shown in Figure 10. The results are very similar to those for the Cu^{2+} doped samples; the peak at ∼4 Å decreases in intensity with increasing annealing temperature. This again suggests that the dopant is moving to disordered regions, probably in the surface regions of the crystallites.

There is some support for the view that the Fe^{3+} ions segregate to the surface of the crystallites from the EXAFS of the nominally 10 mol % doped sample. The effect of annealing

TABLE 2: EXAFS Results for Doped Nanocrystalline Tin Oxide

	X-ray for SnO_2		Cu K-edge EXAFS of 5% Cu−SnO_2[a]			Fe K-edge EXAFS of 5% Fe−SnO_2[b]		
atom	CN	*R*/Å	CN	*R*/Å	*A*/Å^2	CN	*R*/Å	*A*/Å^2
O	2	2.045	6	1.995	0.017	6	2.014	0.008
O	4	2.088						
Sn	2	3.185	2	3.150	0.013	2	3.144	0.011
O	4	3.594	4	3.618	0.011	4	3.460	0.050
Sn	8	3.708	8	3.637	0.018	8	3.688	0.014
				$R = 25.68\%$			$R = 35.30\%$	

[a] The crystallographic data for CuO[40] show the shells around Cu^{2+} are as follows (number of atoms, atom type, distance/Å): 2, O, 1.951; 2, O, 1.961; 2, O, 2.781; 4, Cu, 2.900; 4, O, 3.083; 2, Cu, 3.172; 2, O, 3.408; 2, Cu, 3.421; 2, O, 3.580; 2, Cu, 3.749; 2, O, 3.873. [b] The crystallographic data for Fe_2O_3[41] show the shells around Fe^{3+} are as follows: (number of atoms, atom type, distance/Å): 3, O, 1.947; 3, O, 2.110; 1, Fe, 2.893; 3, Fe, 2.969; 3, Fe, 3.363; 3, O, 3.395; 3, O, 3.594; 6, Fe, 3.702; 3, O, 3.787; 1, Fe, 3.982.

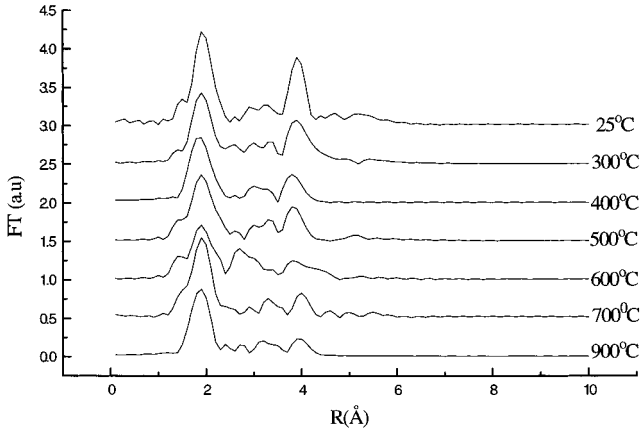

Figure 7. Fourier transforms of nominally 5 mol % Cu doped SnO_2 heated for 1 h at high temperatures. The heating temperatures are listed beside each plot. For clarity the plots have been shifted by 0.5 on the *y*-axis.

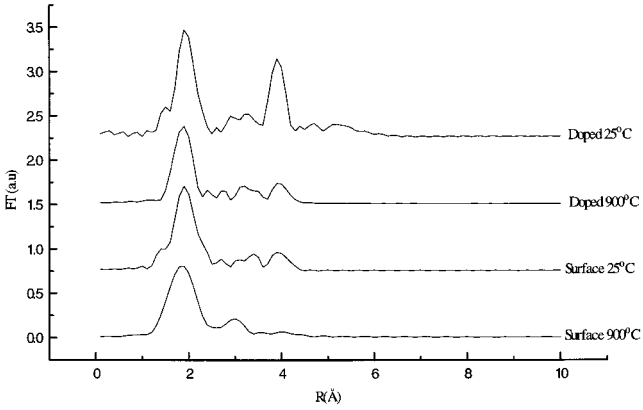

Figure 8. Fourier transforms of bulk and surface Cu doped SnO_2 heated for 1 h at high temperatures. The sample type and heating temperatures are listed beside each plot. For clarity the plots have been shifted by 0.75 on the *y*-axis.

for 1 h at 400 and 900 °C on the EXAFS of this sample is shown in Figure 11. After the sample is annealed at 400 °C, the peak at 4 Å is reduced in amplitude but the general shape of the Fourier transform is like the room temperature sample. In contrast, heating to 900 °C produced a very different Fourier transform with a complex series of peaks between 3 and 5 Å. This corresponds to the precipitation of iron oxide, and a rough fit to the data can be made with Fe_3O_4 as a model. More direct evidence for the formation of iron oxide is the simple observation that after the 900 °C anneal the sample turned to a dark reddish-brown color.

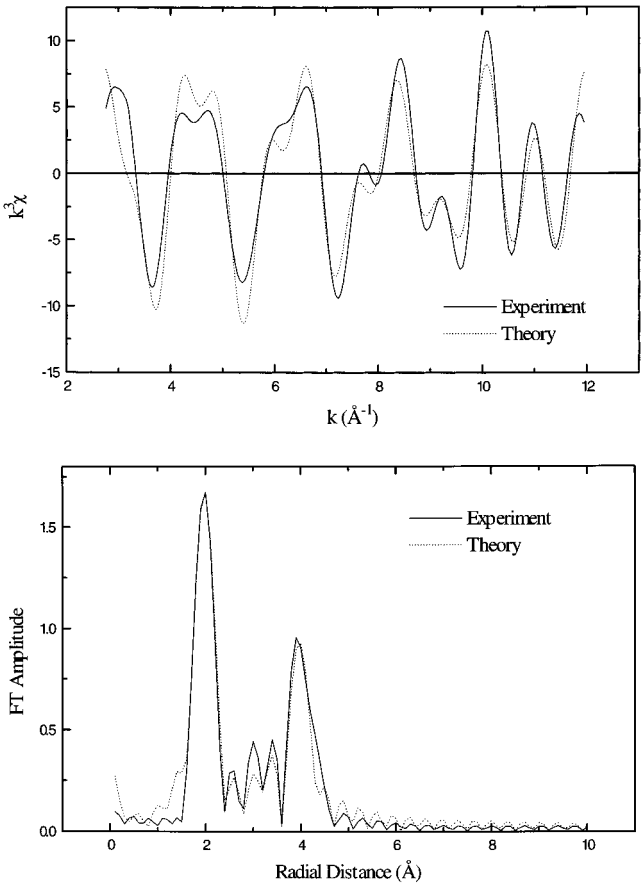

Figure 9. Fe K-edge EXAFS spectrum (k^3-weighted) for a nanocrystalline sample of nominally 5 mol % Fe doped tin oxide (a, top) and the corresponding Fourier transform (b, bottom) corrected with the phase shift of the first shell. The experimental data are the solid line, and the best fit is the dotted line.

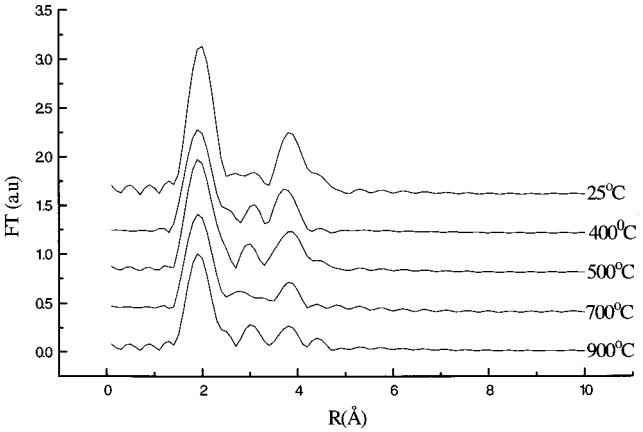

Figure 10. Fourier transforms of nominally 5 mol % Fe doped SnO_2 heated for 1 h at high temperatures. The heating temperatures are listed beside each plot. For clarity the plots have been shifted by 0.5 on the *y*-axis.

4. Discussion

The present work shows that the conventional sol−gel route to SnO_2 produces nanocrystalline material with an average particle size of 2−3 nm, as determined by XRPD. This is consistent with previous work,[27−29] although the final particle size is dependent on the precise preparation conditions. The EXAFS of the pure SnO_2 is typical of a nanocrystalline material

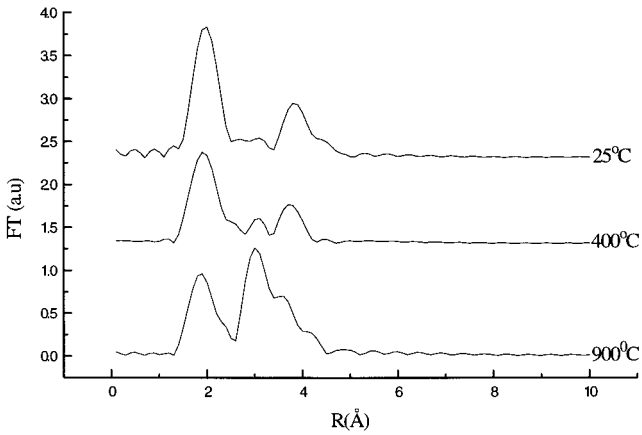

Figure 11. Fourier transforms of nominally 10 mol % Fe doped SnO_2 heated for 1 h at high temperatures. The sample type and heating temperatures are listed beside each plot. For clarity the plots have been shifted by 0.75 on the *y*-axis.

with reduced intensities in the Fourier transform for the peaks from the outer coordination shells. As shown in Table 1, the EXAFS can be fitted with coordination numbers fixed at the crystallographic values for bulk SnO_2 or by allowing the coordination numbers to vary in the least-squares iteration. The latter approach gives a slightly better fit with coordination numbers that are consistent with the crystallite size. In addition the Debye−Waller factors are not very much larger than those for the bulk material. Therefore a picture emerges of nanocrystals in which the level of dynamic and static disorder is not very different from that in large, bulk crystals.

The SnO_2 nanocrystals readily grow at quite moderate temperatures, as shown in Figure 3, and in agreement with previous work.[38] In pure SnO_2 growth is evident at 400 °C and must begin at even lower temperatures. This has implications for the use of nanocrystalline SnO_2 in gas sensors. The sensitivity has an inverse relationship to particle size and is highest for crystallites less than 10 nm diameter, the order of the Debye length in SnO_2.[38] A compromise therefore has to be reached, if possible, where the temperature of sensor operation is sufficient to give a sensitivity to gas without crystallite growth. Doping with Cu^{2+} and Fe^{3+} restricts the crystallite growth. Other workers[38] have found that most dopants, mainly cations, in nanocrystalline SnO_2 restrict grain growth, while a few others, notably Co, have the opposite effect, assisting growth. It has been proposed that the improved sensitivity of SnO_2 gas detectors imparted by dopants is due at least in part to the dopants restricting the grain growth.[38]

The present EXAFS studies clearly show that in the freshly prepared sol−gel nanocrystals doped with Cu^{2+} and Fe^{3+} the dopants are predominantly situated on Sn^{4+} sites in the SnO_2 lattice and not on the surface of the nanocrystals. Evidence for this assertion is the detailed fitting of the EXAFS data for these samples and the comparison with the EXAFS of surface doped samples. In a recent study of Cu^{2+} doped SnO_2 (at nominally 0.08 mol % doping) prepared by similar methods to those used in the present work, the location of the dopant was investigated by EPR and electron spin−echo envelope modulation (ESEEM) spectroscopy.[31] This work indicated there were two major types of Cu^{2+} species: species A which was attributed to a surface hydrated cation and species B which was assigned to Cu^{2+} in the SnO_2 matrix. A quantitative interpretation of the spectra in terms of the relative amounts of Cu^{2+} in the two sites was not given. In the directly doped sample both species A and B were present; the amount of the latter varied from preparation to preparation but was present in significant amounts which increased after calcination at 573 K. In contrast, in surface doped samples species B only occurred after calcination. It was therefore assumed that calcining both directly doped and surface doped samples caused the Cu^{2+} to enter the SnO_2 lattice.

It is difficult to resolve some of the differences between the EPR/ESEEM studies of Cu^{2+} doped SnO_2 and the present EXAFS work. Both investigations show that the sol−gel route leads to incorporation of some Cu^{2+} into the SnO_2 lattice. A small amount of surface Cu^{2+} in the freshly prepared material would be essentially invisible in the EXAFS. It would effectively lower the Debye−Waller factors for the outer shells in the EXAFS fits. The similarity of these factors for the Cu^{2+} doped and pure SnO_2 nanocrystals (see Tables 1 and 2) suggests that the amount of surface Cu^{2+} is small. The major difference in the two investigations is the effect of calcining the samples: the EPR/ESEEM indicating Cu^{2+} incorporation into the lattice and the present work suggesting a relocation of Cu^{2+} in surface regions of the crystallites. One possible explanation is the difference in the concentrations of Cu^{2+} in the two studies, about 1 order of magnitude. At the lower concentration used in the EPR/ESEEM work the Cu^{2+} may be stable within the SnO_2 lattice. It is difficult to refute the present EXAFS studies which indicate that the Cu^{2+} moves out of the SnO_2 lattice on heating. The simplest explanation is that the Cu^{2+} becomes located in the surface regions of the crystallites. This would be consistent with the similarity of the EXAFS for the sol−gel sample heated at 900 °C and the unheated surface doped sample. In addition, the restricted crystallite growth rate on heating of the Cu^{2+} doped nanocrystals compared to pure SnO_2 is indicative of the dopant affecting the surface of the crystallites.

The explanations presented above for the experiments on the Cu^{2+} doped SnO_2 apply to the experiments on Fe^{3+} doped SnO_2. The EXAFS results show that in the freshly prepared nanocrystals the Fe^{3+} is located predominantly on Sn^{4+} sites in the SnO_2 lattice and that heating causes the movement of the dopant to the surface. The precipitation of iron oxide on heating the nominally 10 mol % Fe^{3+} doped SnO_2 at 900 °C, shown by the EXAFS and the color change of the sample, is further good evidence that the dopant is relocated in the surface regions.

Interesting questions that are not fully resolved in the present work are, why are the dopants located on lattice sites in the freshly prepared nanocrystals, why do they relocate on surface sites on heating the samples, and what is the mechanism by which the nanocrystals grow? A feature of nanocrystals is their higher solubility limit for impurities, and this has been noted in the case of SnO_2 for solutions of Eu^{3+}.[28] The present work suggests these solutions are metastable and precipitate the dopant on heating. The migration process of the dopants to the surface is presumably by translational diffusion. Although the diffusion coefficients of cations in oxides are very low,[39] the distances that the dopants need to move to reach the surface are small in nanocrystals, the order of a few lattice spacings. An investigation of the growth mechanism of SnO_2 and the role of dopants in restricting growth would form an interesting and useful study, particularly for the design of gas sensors.[38]

5. Conclusions

This work has used a combination of EXAFS and XRPD to characterize pure and doped SnO_2 nanocrystals prepared by a conventional sol−gel route. The as-prepared samples have a crystallite size of 2−3 nm. The Sn K-edge EXAFS of pure SnO_2 nanocrystals is consistent with the crystallite size and indicates that the nanocrystals have a similar level of static and dynamic disorder to that found in bulk SnO_2. On heating the

nanocrystals of pure SnO_2 show the clear onset of growth around 400 °C. EXAFS measurements at the dopant K-edges in 5 mol % Cu^{2+} and Fe^{3+} doped SnO_2 nanocrystals show that the dopants in the freshly prepared sol−gel materials are located on Sn^{4+} sites in the SnO_2 lattice. Heating these samples causes distinct changes in the EXAFS which have been interpreted as the dopant moving to the surface regions of the crystallites. In the case of a nominal 10 mol % Fe^{3+} doped sample, heating for 1 h at 900 °C caused the precipitation of iron oxide from the sample.

Acknowledgment. We are proud to dedicate this paper to Professor Sir John Meurig Thomas FRS to mark his 65th birthday. Over many years we have benefitted from his sound advice and enthusiastic encouragement. We wish to thank the EPSRC and CCLRC for providing support for the use of the Daresbury facilities in the present work. An award of a CASE studentship by HSE (Sheffield) and EPSRC to S.R.D. is gratefully acknowledged. We are indebted to Dr. S. C. Thorpe at the HSE for his continued interest and support of the sensors research programs at Kent. We also thank the Daresbury Laboratory staff, particularly Drs. A. J. Dent and F. W. Mosselmans, for assistance with the synchrotron experiments. We are grateful to Ernst Richter for help with the initial investigations on the preparation of nanocrystals.

References and Notes

(1) Gleiter, H. *Adv. Mater.* **1992**, *4*, 474.
(2) Henglein, A. *Chem. Rev.* **1989**, *89*, 1061.
(3) Weller, H. *Angew. Chem., Int. Ed. Engl.* **1993**, *32*, 41.
(4) See, for example, papers in the special issue of: *Chem. Mater.* **1996**, *8* (8).
(5) Stark, J. V.; Park, D. G.; Lagadic, I.; Klabunde, K. J. *Chem. Mater.* **1996**, *8*, 1904.
(6) Stark, J. V.; Klabunde, K. J. *Chem. Mater.* **1996**, *8*, 1913.
(7) Koper, O.; Lagadic, I.; Klabunde, K. J. *Chem. Mater.* **1997**, *9*, 838.
(8) Lantto, V. In *Gas Sensors: Principles, Operations and Developments*; Sberveglieri, G., Ed.; Kluwer: Dordrecht, The Netherlands, 1992; p 117.
(9) Williams, D. E. In *Solid State Gas Sensors*; Moseley, P. T., Tofield, B. C. Eds.; Adam Hilger: Bristol, U.K., 1987; p 71.
(10) Taguchi, N. U.K. Patent Specification, 1280809, 1970.
(11) Chatelon, J. P.; Terrier, C.; Bernstein, E.; Berjoan, R.; Roger, J. A. *Thin Solid Films* **1994**, *247*, 162.
(12) Ansari, S. G.; Boroojerdian, P.; Kulkarni, S. K.; Sainkar, S. R.; Karekar, R. N.; Aiyer, R. C. *J. Mater. Sci.: Mater. Electron.* **1996**, *7*, 267.
(13) Demarne, V.; Sanjines, R. In *Gas Sensors: Principles, Operations and Developments*; Sberveglieri, G., Ed.; Kluwer: Dordrecht, The Netherlands, 1992; p 89.
(14) Barbi, G. B.; Santos, J. P.; Serrini, P.; Gibson, P. N.; Horrillo, M. C.; Manes, L. *Sens. Actuators, B* **1995**, *24−25*, 559.
(15) Fuller, M. J.; Warwick, M. E. *J. Catal.* **1974**, *34*, 445.
(16) Fuller, M. J.; Warwick, M. E. *J. Catal.* **1976**, *42*, 418.
(17) Harrison, P. G.; Harris, P. Eur. Patent 0328373B1, 1993.
(18) Maekawa, T.; Tamaki, J.; Miura, N.; Yamazoe, N. *J. Mater. Chem.* **1994**, *4*, 1259.
(19) Koningsberger, D. C.; Prins, R. *X-ray Absorption. Principles, Applications, Techniques of EXAFS, SEXAFS and XANES*; Wiley: New York, 1988.
(20) Gurman, S. J. In *Applications of Synchrotron Radiation*; Catlow, C. R. A., Greaves, Eds.; Blackie: Glasgow, 1993; p 140.
(21) Chadwick, A. V. In *Applications of Synchrotron Radiation*; Catlow, C. R. A., Greaves, G. N., Eds.; Blackie: Glasgow, 1993; p 171.
(22) Chadwick, A. V.; Russell, N. V.; Whitham, A. R.; Wilson, A. *Sens. Actuators, B* **1994**, *18*, 99.
(23) Russell, N. V.; Chadwick, A. V.; Wilson, A. *Nucl. Instrum. Methods Phys. Res., B* **1995**, *97*, 575.
(24) Chadwick, A. V.; Harsch, A.; Russell, N. V.; Tse, K. F.; Whitham A. R.; Wilson, A. *Radiat. Eff. Defects Solids* **1995**, *137*, 1277.
(25) Nitsche, R.; Winterer, M.; Croft, M.; Hahn, H. *Nucl. Instrum. Methods Phys. Res., B* **1995**, *97*, 127.
(26) Brook, H. C.; Chadwick, A. V.; Kennedy, K. M.; Morgante, N.; Rafeletos, G.; Tomba, A.; Roberts, M. A. *Mater. Sci. Forum* **1997**, *239−241*, 687.
(27) Briois, V.; Santilli, C. V.; Pulcinelli, S. H.; Brito, G. E. S. *J. Non-Cryst. Solids* **1995**, *191*, 17.
(28) Brito, G. E. S.; Ribeiro, S. J. L.; Briois, V.; Dexpert-Ghys, J.; Santilli, C. V.; Puncinelli, S. H. *J. Sol-Gel Sci. Technol.* **1997**, *8*, 261.
(29) Brito, G. E. S.; Briois, V.; Puncinelli, S. H.; Santilli, C. V. *J. Sol-Gel Sci. Technol.* **1997**, *8*, 269.
(30) Chadwick, A. V. *Solid State Ionics* **1993**, *63−65*, 721.
(31) Matar, K.; Zhao, D.; Goldfarb, D.; Azelee, W.; Daniel, W.; Harrison, P. G. *J. Phys. Chem.* **1995**, *99*, 9966.
(32) Kanai, H.; Mizutani, H.; Tanaka, T.; Funabaki, T.; Yoshida, S.; Takano, M. *J. Mater. Chem.* **1992**, *2*, 703.
(33) Klug, H. P.; Alexander, L. E. *X-ray Diffraction Procedures*; Wiley: New York, 1974.
(34) Dent, A. J.; Oversluizen, M.; Greaves, G. N.; Roberts, M. A.; Sankar, G.; Catlow, C. R. A.; Thomas, J. M. *Physica* **1995**, *209*, 253.
(35) Binsted, N.; Campbell, J. W.; Gurman, S. J.; Stephenson, P. C. *SERC Daresbury Program Library*; Daresbury Laboratory: Warrington, Cheshire, U.K., 1992.
(36) Seki, H.; Ishizawa, N.; Mizutani, N.; Kato, M. *Yogyo Kyokai Shi* **1984**, *92*, 219.
(37) Goniakowski, J.; Holender, J. M.; Kantorovich, L. N.; Gillan, M. J.; White, J. A. *Phys. Rev. B* **1996**, *53*, 957.
(38) Xu, C.; Tamaki, J.; Miura, N.; Yamazoe, N. *Chem. Lett.* **1990**, 441.
(39) Philibert, J. *Atom movements: diffusion and mass transport in solids* (English translation by S. J. Rothman); Les Editions de Physique: Paris, 1991.
(40) Brese, N. E.; O'Keeffe, M.; Ramakrishna, B. B. L.; Von Drele, R. B. *J. Solid State Chem.* **1990**, *89*, 184.
(41) Perkins, D. A.; Attfield, P. A. *J. Chem. Soc., Chem. Commun.* **1991**, *4*, 229.